View metadata, citation and similar papers at core.ac.uk

brought to you by CORE

provided by PORTO@iris (Publications Open Repository TOrino - Politecnico di Torino)


POLITECNICO DI TORINO
Repository ISTITUZIONALE

# Sensitivity Analysis of a Neural Network based Avionic System by Simulated Fault and Noise Injection

*Original*
Sensitivity Analysis of a Neural Network based Avionic System by Simulated Fault and Noise Injection / Brandl, Alberto; Battipede, Manuela; Gili, Piero; Lerro, Angelo. - ELETTRONICO. - (2018), pp. 1-19. ((Intervento presentato al convegno AIAA SciTech Forum tenutosi a Kissimmee, Florida, USA nel 8-12 January 2018.

*Availability:*
This version is available at: 11583/2699969 since: 2019-03-11T19:00:55Z

*Publisher:*
AIAA

*Published*
DOI:10.2514/6.2018-0122

*Terms of use:*
openAccess

This article is made available under terms and conditions as specified in the corresponding bibliographic description in the repository

*Publisher copyright*
default_conf_editorial

-

(Article begins on next page)

04 August 2020

# Sensitivity Analysis of a Neural Network based Avionic System by Simulated Fault and Noise Injection

Alberto Brandl*
*Politecnico di Torino, Corso Duca degli Abruzzi, 24, 10129, Turin, Italy*

Manuela Battipede†
*Politecnico di Torino, Corso Duca degli Abruzzi, 24, 10129, Turin, Italy*

Piero Gili‡
*Politecnico di Torino, Corso Duca degli Abruzzi, 24, 10129, Turin, Italy*

Angelo Lerro§
*AeroSmart s.r.l., Caserta, Italy*

**The application of virtual sensor is widely discussed in literature as a cost effective solution compared to classical physical architectures. RAMS (Reliability, Availability, Maintainability and Safety) performance of the entire avionic system seem to be greatly improved using analytical redundancy. However, commercial applications are still uncommon. A complete analysis of the behavior of these models must be conducted before implementing them as an effective alternative for aircraft sensors. In this paper, a virtual sensor based on neural network called Smart-ADAHRS (Smart Air Data, Attitude and Heading Reference System) is analyzed through simulation. The model simulates realistic input signals of typical inertial and air data MEMS (Micro Electro-Mechanical Systems) sensors. A procedure to define the background noise model is applied and two different cases are shown. The first considers only the sensor noise whereas the latter uses the same procedure with the operative flight noise. Flight tests have been conducted to measure the disturbances on the inertial and air data sensors. Comparison of the Power Spectral Density function is carried out between operative and background noise. A model for GNSS (Global Navigation Satellite System) receiver, complete with constellation simulator and atmospheric delay evaluation, is also implemented. Eventually, a simple multi-sensor data fusion technique is modeled. Results show a good robustness of the Smart-ADAHRS to the sensor faults and a marginal sensitivity to the temperature-related faults. Solution for this kind of degradation is indicated at the end of the paper. Influences of noise on input signals is also discussed.**

## I. Introduction

During last years a lot of research has shown how virtual sensors can play a crucial role in an avionic system [1]. A sensor is considered virtual when the output comes from a software evaluation in place of a physical measurement. This kind of architecture can be used in a lot of fields beyond aeronautics and it seems to offer a valid solution to the reliability issues. Examples of non-aeronautical applications can be found in Ref. [2] and [3]. In the first case, a virtual pressure sensor has been developed for the evaluation of the combustion chamber pressure in a diesel engine. This would allow the design of closed-loop control without using expensive physical sensors. The latter one shows a virtual surface temperature sensor for multi-zone air-conditioning systems. In both articles, the virtual sensing is considered an effective low cost technique. Because of their potentiality, a considerable amount of literature has been published on virtual sensors for aeronautical systems, where some problems arise on the design of the sensor architectures [4, 5]. In fact, Samy and Da-Wei [1] state that cost, weight and space restrictions may prevent to apply physical sensor redundancy on UAVs. Actually, most of the current projects focus on SFDIA (Sensor Fault Detection, Isolation and Accommodation)

*PhD student, DIMEAS, alberto.brandl@polito.it
†Associate Professor, DIMEAS, manuela.battipede@polito.it
‡Associate Professor, DIMEAS, piero.gili@polito.it
§AeroSmart s.r.l., angelo.lerro@aerosmartsrl.it

solutions. In those cases, there is a main sensor, which can be physical or virtual, coupled with an architecture able to detect its faults and accomodate them, and it is quite common to see virtual sensors applied as analytical redundancy. Here, solutions mainly concern parameter estimation and state observation, usually implemented as linear systems or model-based techniques. Nonlinear estimation is also implemented by means of soft-computing techniques as ANN (Artificial Neural Network) or GA (Genetic Algorithm). Refer also to Ref. [6–9] for additional details.

Although the promising introduction, the estimated measurement could suffer from faults on preceding systems, applied as input signals. Currently, commercial applications of virtual sensors are still hard to find. An example can be seen in Ref. [10] where a fuzzy logic is implemented for multiple faults detection.

The reliability analysis of such a system is a crucial phase to define the practical use of virtual sensing. To assess RAMS (Reliability, Availability, Maintainability and Safety) performance on complex systems or even on systems of systems, different techniques have been developed in the past. Fault injection, for instance, consists in the reproduction of a fault on the input signals or on the equipment itself in order to observe the consequent evolution. This can be done hardware-based, software-based or even in a simulated environment [11–15]. A framework called RAMSAS has been depicted as a complement to classical RAMS analysis in Ref. [16] and [17].

This paper shows a sensitivity analysis for a nonlinear virtual sensor to degradation of the input signals both in terms of noise and faults. The entire evaluation has been conducted on a simulated environment using data from static measurements and flight tests. The analyzed sensor is called Smart-ADAHRS (Smart Air Data, Attitude and Heading Reference System), which is an innovative avionic system able to estimate the aerodynamic angles of an aircraft without using state-of-the-art external physical sensors. This patented technique [18] has been investigated during previous research [19–25]. This paper shows that a detailed simulation of the entire architecture can help to define when a complex system as Smart-ADAHRS fails. Moreover, this kind of analysis can help to define the technical requirements for the input signals. Section II provides a background on the typical characteristics of sensors as non-linearity, noise and faults. Section III shows how they have been implemented in the simulated environment. Section IV shows some results obtained on the model and, at the end of the paper, Section V reports the conclusion over the sensitivity of Smart-ADAHRS to noise and faults.

## II. Background

The word "sensor" loosely describes a lot of very different systems. Every equipment able to translate a physical quantity to any kind of related information could be referred to as a sensor. Here, the focus is on kinematic and air data measurements, which are the typical led on an aircraft. Recently, a lot of interest has been focused around MEMS (Micro Electro-Mechanical Systems), being currently cheaper and requiring less maintenance than the classical IMU (Inertial Measurement Unit). However, the model described in this paper can simulate non-MEMS sensors as well, except for the background noise which is tailored for MEMS.

Another kind of sensor, considered in this paper, is the GNSS (Global Navigation Satellite System) receiver, which has a completely different architecture. In this case a theoretical number of 4 satellites in view from a constellation is needed in order to obtain, generally by means of trilateration, the position of the radio receiver. Different solutions have been developed during the last decades and a detailed description can be seen in Ref. [26]. The model should be able to describe the entire family of GNSS equipment without being strictly related to the internal architecture. The group of inertial sensors, typically an accelerometer and a gyroscope for each Body axis, in some case coupled with a magnetometer, is generally referred as AHRS (Attitude and Heading Reference System) and is integrated with a GNSS receiver to overcome drift issues. Different levels of integration exist as reported in Ref. [27]. The increased complexity of a deep integration results in an increased accuracy of the final state estimation. Moreover, it provides an improved robustness compared with a loose integrated system. Commonly, these techniques involve using state-observer techniques as the most famous KF (Kalman Filter) [28, 29].

The focus of this paper is to define a worst case scenario, where the virtual sensor is still able to define a reliable output. For this reason, the loosely coupled architecture, which is the simplest one, has been considered. In fact, deep integration schemes do not meet the conservative approach of this paper.

### A. Sensors with relevant dynamical behavior

This section considers all those kinds of sensors that resemble dynamical systems. For sake of clarity, the majority of inertial and air data sensors can be modeled as dynamical systems because of their architecture. In fact, a typical force, stress or position sensor is based on the measurements of some static or dynamical property of an internal structure, which might be a beam, a fork, a wheel or any other structure that can be subjected to the physical quantity to measure.

The position and angular sensors typically implemented in actuators can be modeled as dynamical system as well. Generally speaking, a sensor can be divided in four main parts: the probe, the transducer, the conditioning system and the Analog-to-Digital converter. Unfortunately, the output of a sensor undergoes to a lot of non-linearities. A brief classification of the probe & transducer characteristics could be the following:

- *Static characteristics* consider the effects on scale factor (also called sensitivity), resolution, deviation from the theoretical linearity, threshold and dead-zone, hysteresis, bias and asymmetry;
- *Dynamic characteristic* consider the frequency response of the system and hence natural frequency, bandwidth, hysteresis, repeatability and noise.

*1. Hysteresis model*

Hysteresis, despite of its diffusion in a lot of physical phenomena, is not an easy behavior to model. Three main properties describe the histeretic system:

1) Rate dependency/independency: the time derivative of the input affects or not the trajectory on the configuration space
2) Congruency: minor loops with different output are congruent
3) Wiping-out: only the last extreme input value define the current hysteretic loop

Several models have been investigated in literature, for instance the Preisach model and its expansions [30, 31] or the Bouc-Wen model [32]. Here, the Wang-Willatzen model [33] is implemented because, despite for its drawbacks, is easily implementable with slight modification from a classical damper-spring-mass model. Eq. (1) allows to expand the common mass-spring-damper model to an hysteretic behavior

$$m\ddot{u} + c\dot{u} + \alpha u + \beta u^3 + \gamma u^5 = F(t) \tag{1}$$

where $m$ is the equivalent mass, $c$ is the damping coefficient, $\alpha$ is the linear stiffness coefficient, $\beta$ and $\gamma$ are the nonlinear stiffness coefficients and $F$ is the forcing input. The fact that descending trajectory does not replicate the rising one is obtained with jumps in the force scalar potential. Setting properly the values for stiffness and damping the trajectory follows an histeretic path. Further studies enlightened the fact that the model is rate-dependent, as can be seen in Fig. 1. Moreover, the fifth-degree term brings to additional local minima on the scalar potential, corresponding to extra stable equilibrium positions on the $u\,F$- plane. This eventually results in an attraction to the origin behavior, also showed in Fig. 1. This phenomena can be reduced tuning the coefficients of the polynomial.

However, the typical hysteresis of a COTS (Commercial Off-The-Shelf) sensor is very low. For this reason, the authors consider this model enough accurate for the simulation. The model allows also to run a linear static model and a second order linear model. A right selection of the model can greatly affect the simulation time.

*2. Background noise*

Various work has been done in literature to evaluate noise in gyroscopes and accelerometers. Refer to Ref. [34] and [35] for detailed descriptions of typical background noises in MEMS and inertial sensors. As Fig. 2 from Ref. [34] shows, the typical single-sided PSD (Power Spectral Density) for accelerometers and gyroscopes can be divided in:

1) Angle random walk (Velocity random walk for accelerometers), N, measure unit of the time integral of the sensor output times the square root of frequency, very close to white noise. The counter-intuitive name comes from the fact that this part will generate a random walk on the time integral of the sensor signal.
2) Rate random walk (Acceleration random walk for accelerometers), K, same measure unit of the sensor output times the square root of frequency, very close to brown noise
3) Bias stability (same measure unit as sensors output), B, usually modeled as pink noise

The accurate simulation of a sensor would require a complete analysis of the background noise. Unfortunately, values describing in details the PSD structure are not always available.

### B. GNSS

Global Navigation Satellite System (GNSS) is a system that provides geo-spatial positioning using a constellation of satellites potentially supported by ground stations called pseudolites. This constellation is usually in Mean Earth Orbit (MEO) as a trade off between the minimum number of satellite needed for coverage in geostationary orbit and a greater number of satellite in lower and more reachable orbit. Each satellite sends information about satellites position at a

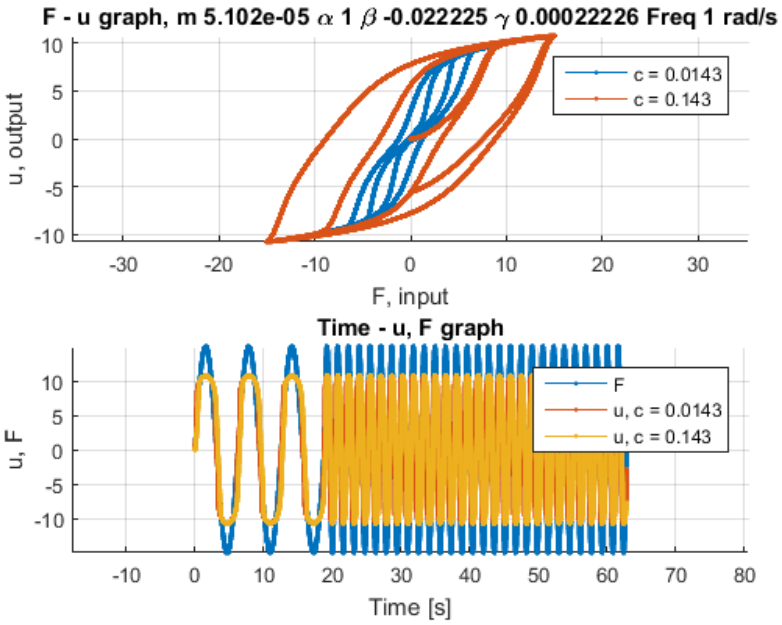


**Fig. 1 Attraction of the origin, effects of the input frequency** (1 rad/s, 4 rad/s) **and damping coefficient, all measure units are congruent**

given time and the receiver can obtain its own position by means of triangulation or trilateration. Some GNSS receiver are able to give also an estimation of the receiver velocity vector.

Because INS (Inertial Navigation System) suffers from integration error, the GNSS is often integrated in multi-sensor data fusion techniques with INS. The output of a GNSS receiver, which has a low sampling rate around 1 s, is used to reset the integration error of the INS, which runs at an higher sampling rate. The GNSS architecture is so different from inertial and air data sensor that the description in Section II is not suitable for modeling its behavior. A proper model is needed. A lot of work has been done in literature and several commercial simulators exist. The simple addition of a white noise to the output is not enough to consider the degradation of the signal, for instance, coming from the geometry of the in-view satellites. At the same time, atmospheric delay should be modeled in order to get an accurate simulation. There is no place for a complete description of the GNSS system, please refer to Ref. [26] for a more detailed work.

Errors acting on this kind of avionic equipment can be divided in deterministic, observation and random errors. Deterministic source of errors are:

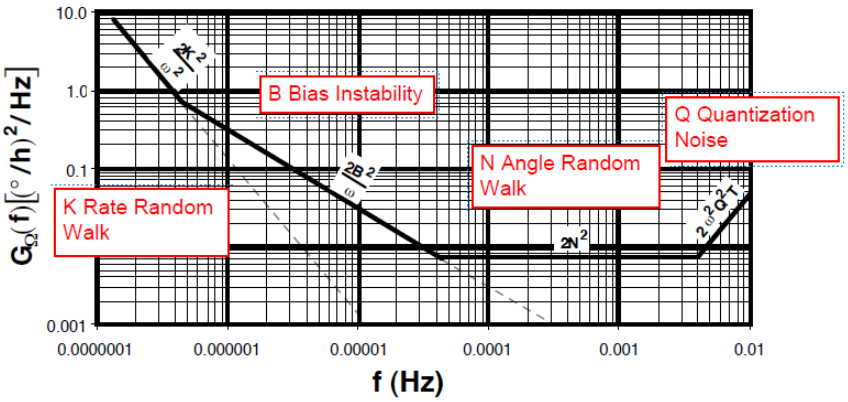


**Fig. 2 Typical Single Sided PSD for a MEMS sensor. (from [34])**

1) Clock: one of the greatest source of deterioration, may be divided in receiver clock and satellite clock. Whereas the satellite has a very stable and accurate rubidium atomic clock, the receiver has usually a cheaper one. See Ref. [36], [37] and [38] for literature around oscillator and clock modeling;
2) Orbit model error: coming from the estimation of the satellite position, they typically reflect a ranging error of 1 m;
3) Path bending: it concerns the path followed by the radio-magnetic wave according to the Fermat's principle. If elevation angle is higher than 10° this effect is quite small. Moreover, GNSS receiver usually drops satellites with elevation angle lower than a threshold value from 5° to 10°;
4) Tropospheric refraction: In spite of its name, it actually accounts for the first 40 km of the atmosphere with an effect between 2.5 m and 15 m, depending on the elevation angle;
5) Ionospheric refraction: frequency dependent effect, usually estimated also in civil receivers by means of code-less tracking. Ranging error around 3 m;
6) SA (Selective Availability): algorithm applied until May 1, 2000 to degrade position accuracy of civil receiver, now deactivated. Not implemented in the simulator.

Observation errors:

1) Multipath: signal reflected by ground or external structure of the aircraft is delayed and receiver cannot distinguish between the original and the reflected one. Errors around 10 m might be obtained with C/A code;
2) Receiver electronics: internal noise that acts on reference oscillators and lock circuit;
3) Electromagnetic interference: it might be voluntary as jamming or not, here not modeled;
4) Antenna position: difference between ideal center of antenna and receiver virtual point, very little effect, here not modeled.

Random errors:

1) Accuracy of PRN (Pseudorandom Noise) codes: receiver can reproduce the PRN code with a limited precision (usually around 1 % of the chip rate)
2) Frequency determination: phase shift may bring to error on Doppler measurements

The relative geometry of the satellites in view and the receiver affects the final position accuracy. In fact, when the measurements are not ideal, the receiver position error $\Delta X$ is related to the range measurement error $\Delta\rho$ by the Eq. 2.

$$\Delta X = \mathrm{DOP}\Delta\rho \tag{2}$$

where DOP stands for Dilution of Precision and depends only on the relative geometry of the constellation in view. See [26] for additional details. DOP can be expressed as GDOP (Geometric DOP), which considers the overall effect or by PDOP (Position DOP), HDOP (Horizontal DOP), VDOP (Vertical DOP) and TDOP (Time DOP).

### C. Smart-ADAHRS

Aerodynamic angles define the relative orientation of the so-called Air Trajectory reference frame with respect to the Body axes of the vehicle. These angles are strictly related to the aerodynamic forces acting on the aircraft and consequently to dynamics of the vehicle itself. AOA (Angle of Attack) and AOS (Angle of Sideslip) are usually applied as feedback signals in aeronautical control systems. Current state-of-the-art ADS (Air Data System) are based on physical external sensors with hardware redundancy. In [23] the advantages of using a ANN-based ADS on UAV are shown. Fig. 3 provides the general schematic of the Smart-ADAHRS, although some modifications can be applied depending on the input sensors. For instance, an integrated ADAHRS can be used in place of the AHRS moving the external probe to the corresponding block.

The algorithm is based on splitting the $\alpha$ angle in two parts as follow:

$$\alpha = \alpha_{in} + \Delta\alpha \tag{3}$$

where $\alpha_{in}$ (also reported as $\hat{\alpha}$) can be obtained by means of a small perturbation model and $\Delta\alpha$ is the error of the evaluation. Previous research showed that $\Delta\alpha$ can be obtained with a properly trained NN. The same holds of $\beta$. The architecture selected for the NN is an MLP (Multilayer Perceptron). Various architectures have been analyzed in the past but always focusing on shallow networks of one or two hidden layers with a number of neurons between 10 to 30. The validity of the approach is mathematically proven using the UAT (Universal Approximation Theorem) [39, 40]. In fact, it is proven that any continuous function of $n$ real variables with support in the unit hypercube $[0, 1]^n$ can be uniformly approximated by finite superposition of a fixed, univariate function that is discriminatory.

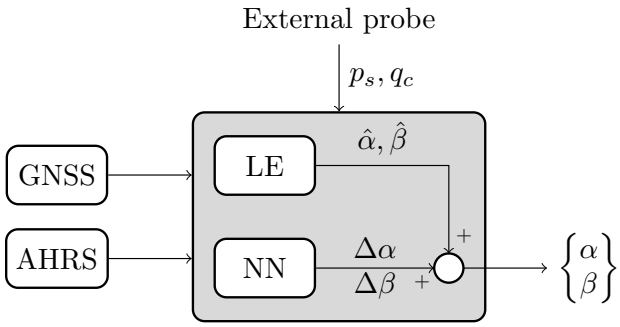


**Fig. 3 General schematic of the Smart-ADAHRS (LE stands for Linear Estimator and NN for Neural Network)**

The main aspects affecting the final results are related to the training operation. In fact, the output of an MLP that minimize the SSE (Sum-of-Squares Error) is the conditional average of the target distribution given the input as in Eq. 4 (see [41, 42]).

$$y_k(\mathbf{x}|\mathbf{w}^*) = \int t_k p(t_k|\mathbf{x})\, dt_k \tag{4}$$

where $\mathbf{x}$ represents a generic input vector, $\mathbf{w}^*$ is the set of weights that minimizes the SSE, $y_k$ and $t_k$ are the output and the target values respectively, and $p(t_k|\mathbf{x})$ represents the conditional density distribution of the target given the input.

This paper addresses the analysis of the regressor in Eq. 5

$$\Delta\alpha = \Delta\alpha(\alpha_{in}, q_c, \dot{q_c}, q, \theta, \phi, n_x, n_z, V_D) \tag{5}$$

where $q_c$ and $\dot{q_c}$ represent the impact pressure and its time derivative respectively, $q$ is the pitch rate, $\theta$ and $\phi$ the pitch and roll angles, $n_x$ and $n_z$ the longitudinal and normal load factors and $V_D$ the component of the velocity along the Down unit vector, according to the NED reference frame.

## III. Methodology

A modular approach is adopted in order to get maximum scalability of the model. Section A covers the modeling of inertial and physical sensor. Although description is mainly focused on MEMS-based sensor, this model is able to represent non-MEMS sensor as well. As previously stated, GNSS receiver needs a properly designed simulator and section B will briefly describe the model implemented for this equipment.

### A. Inertial and physical sensor modeling

Once a sensor with only one degree of freedom (DoF) has been built, the modular approach allows the construction of more complex sensors. Following sections will describe typical behavior of what is generally called "sensor" without specifying what kind of measure is conducted, or architecture is used. These features are hence assigned to properly built subsystems and hence described. The model is divided in *Sensor kernel*, *Real effects generator*, *Failure generator* and *Line noise*. *Sensor kernel* is in turn divided in *Probe & Transducer*, *Conditioning system* and *Analog to Digital Converter*. Although probe and transducer are physically separated, several reasons bring to join them in an equivalent system. Moreover, data-sheets frequently report characteristics of the probe and transducer as if it were a monolithic black box. Hence, from now on they are grouped in a single subsystem. Fig. 4 presents a general schematic of the modeled system. The *Real effects generator* allows to add deterministic and stochastic errors to the measured quantity to represent, for instance, position error or oscillations of the probe. The *Failure generator* generates signals that interacts with the other blocks. For instance, a boolean signal will set to zero the output of the model when the *null output* fault is simulated, or a temperature ramp is placed to the input of the *Sensor kernel* to simulate an increasing temperature.

The resulting model is considered accurate enough for the aim of this paper but it is still executable on a personal laptop. The overall list of the model parameters is reported in Table 1.

At the same time, in order to validate the proposed model, a physical ADAHRS has been used as comparison. Several runs have been conducted to find the proper configuration able to replicate this COTS sensor.

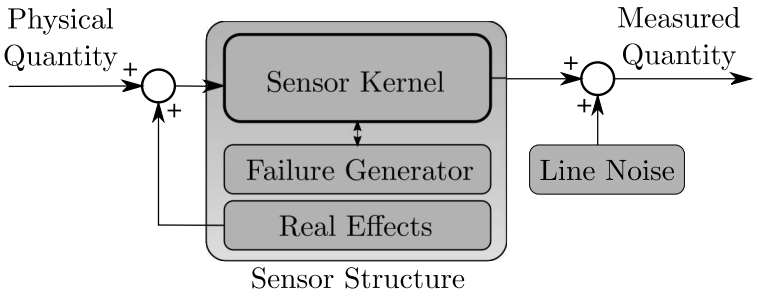


**Fig. 4 General schematic of the sensor subsystem.**

**Table 1 List of the model parameters (dynamical sensor)**

| | |
|---|---|
| Full scale [SU] | Dynamic model equivalent mass [-] |
| Threshold [SU] | Dynamic model equivalent damping coefficient [-] |
| Fixed bias [SU] | Dynamic model equivalent third degree stiffness [-] |
| Bias stability from turn-on to turn-on [SU] | Dynamic model equivalent fifth degree stiffness [-] |
| Bias temperature stability [SU/K] | Natural frequency (phase = −90 deg) [rad/s] |
| White noise input process power [$SU^2$] | Damping factor [-] |
| AR model parameters | Misalignment matrix [-] |
| Scale factor temperature sensibility [%/K] | Floating point precision of ADC [SU] |
| Operating temperature range [K] | Bias compensation (added to the input) |
| Bias reference temperature [K] | Misalignment and sensitivity compensation matrix (left multiplied by (input + bias)) |
| Reference temperature [K] | |

Because the model will implement the ADC (Analog to Digital Converter) directly, the *Quantization error* has not been modeled inside the *Real effects generator*.

To simulate a reliable background noise, the output of the available ADAHRS has been measured with null acceleration and angular rate. This phase is quite delicate because sensors are very sensitive to external inputs. The output has been sampled at 20 Hz. A thumb rule for the definition of the total acquisition time could be seen in Eq. 6 [43].

$$VarV_X(\tau) \leq \frac{4}{T}\int_0^{\infty} R_X^2(\tau)d\tau \tag{6}$$

where $V_X(\tau)$ is an unbiased estimator of the process noise autocorrelation $R_X(\tau)$. Supposing a first order Gauss-Markov process with correlation of 1 s in [43] Park obtained a total sampling period 200 times the process time constant in order to get a 10 % accuracy. The matter is hence the dimension of datalog that is obtained. Supposing to know the process time constant, which is actually unknown, a total acquisition time of about 10 hours is estimated. Anyway, it is quite difficult to avoid any interference or movement in such a long time. Hence, further analysis brought the authors to consider only 2 h recording. At the end of the measurements an AR (Auto Regressive) model has been fitted using the Burg method [44]. The AR model of n-th order is defined as in Eq. 7.

$$X_t = c + \sum_{i=1}^{n} \rho_i X_{t-i} + \varepsilon_t \tag{7}$$

where $c$ is a constant, $\varepsilon_t$ is a Gaussian distributed disturbance with known mean and variance and $\rho_i$ are the parameters of the model, relating the previous values assumed by the random process $X$.

Similar operation has been conducted to measure the operative environment noise. Several time windows coming from flight tests have been selected to fit the AR models. Whereas background noise of the MEMS sensor is related to the electronic noise of the internal architecture, the one in operative scenario concern structural vibrations and

**Table 2 Digital HP filter configuration**

| | |
|---|---|
| Filter architecture | Digital High Pass IIR |
| Filter Order | 4 |
| Passband Frequency | 0.1 Hz |
| Passband Ripple | 1 dB |
| Sample rate | $10 f_s$ where $f_s$ is the signal sampling frequency |

electronic noise from other sources, like the engine, propeller and turbulence. Other disturbances of known frequency and magnitude are contemplated by the model by means of properly designed subsystems. From flight tests executed on 23rd of January 2015 the selection of time windows focused on taxi operations, especially when the aircraft is waiting for clearance.

A notable random walk was been noticed coming from the AR model in case of background sensor noise. For this reason the output of the AR model has been filtered by a digital HP (High Pass) filter to avoid long term modeling error. See Table 2 for details on filter configuration. The effect of this filter is clearly visible in Fig. 5.

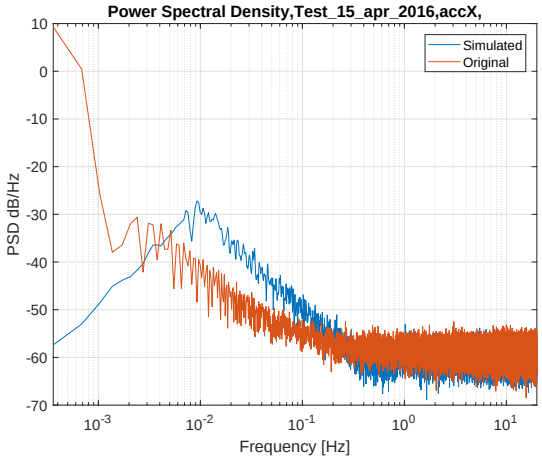


**Fig. 5 Example showing a comparison between the measured background noise PSD and the simulated one for the accelerometers along the X Body axis.**

Eventually, 78 PSDs divided in 39 PSDs from measured data and 39 PSDs from filtered data, have been obtained with corresponding AR parameters using, at first trial, a 10th order model.

This operation has been repeated on two different days obtaining similar results. A moving average behavior has been obtained. Firstly, it was associated to the movement of the ADAHRS, which was supported by a soft layer of foam to filter high frequency vibrations. During the second day of measurements the soft layer had been removed and cable connection had been secured avoiding load on the equipment that could move it. Same behavior was obtained and hence it was considered a consequence of the random walk previously described.

In the end, a long time acquisition of about 15 hours was conducted. Although issues on low frequencies shifted on lower ones, difference on fix quality did not change. At the same time the dimensions of datalog increased. For these reasons, the 2 hours acquisition has been applied in the following analysis.

### B. GNSS receiver modeling

Previous section detailed the model for sensors with relevant dynamical behavior, as air data and inertial sensors. Also the position sensors mounted on an actuator or similar can be simulated with the same model. A GNSS receiver is totally different and a proper model is needed to simulate its behavior. The solution proposed take advantage of a constellation simulator, based on Keplerian orbit, which propagates the orbits determined from an automatic download

**Table 3 List of faults**

| GNSS Receiver faults | Description |
|---|---|
| KF fault | KF stops to update |
| PLL fault | Zero satellites in view |
| Satellite fault | Satellites in view randomly loss |
| Mask angle change | Change the minimum elevation angle (it can be defined depending also on the azimuth angle) |
| **ADAHRS faults** | **Description** |
| Null output | Output signal set to 0 |
| Temperature fault | Temperature increasing with given slope |

of the SEM almanac from the CelesTrak website*. The atmospheric delay has been implemented by means of the Niell Mapping Function [45]. This solution allows to consider, with good accuracy, both the wet and dry components of the delay without using additional surface meteorological data. Eventually, the model evaluates the position of the receiver by means of a EKF (Extended KF), UKF (Unscented KF) or with a linear system. Obviously, the linear system may have only a didactic value being too much inaccurate. General flowchart for the model can be seen in Fig. 6

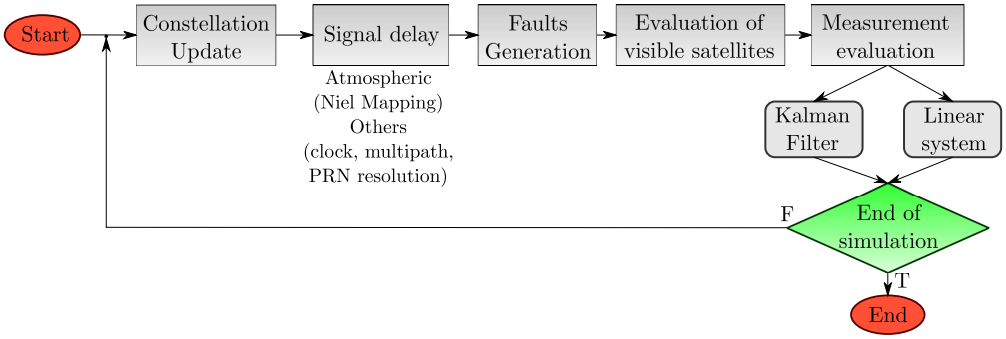


**Fig. 6 General schematic of the GNSS receiver subsystem.**

### C. Integration and fault generation

The outputs of the AHRS and GNSS receiver model have been integrated using a typical KF. This architecture is commonly known as loosely integrated solution and it is considered the simplest and conservative approach. Because the sensitivity analysis should be conducted in a worst case scenario, the simple integration architecture should convince that any better solution will provide greater accuracy and robustness.

Faults are generated on two levels:

- on a functional level, for instance multiplying by zero a signal simulating a *null output* fault;
- in a lower level, for instance eliminating a random number of satellites from the in-view set, generating an increment on the DOP value in an indirect way.

All possible faults are enlisted in Table 3.

## IV. Results

So far, a detailed model for the simulation of the real effects has been depicted. This section will show the output of the Smart-ADAHRS in case of failure injection and realistic noise on the input signals. Two different test cases will be considered. The first case considers only the background noise proper of the sensors. The second one is affected with operative noise recorded during flight tests. A list of faults will be injected. In order to consider in both cases the worst case scenario, and hence actually depict some requirements for the input signals, some of the faults overlap in time. The

*https://celestrak.com/

**Table 4 Simulated sensor faults**

| Sensor | Fault | Event time |
|---|---|---|
| GPS | PLL down | From 16 s to 46 s |
| GPS | Reduced number of visible satellites | From 60 s to 90 s |
| GPS | Kalman Filter down | From 100 s to 130 s |
| AHRS | Accelerometers null output | 150 s |
| AHRS | Accelerometers temperature increase | 50 s |

**Table 5 Accuracy comparison for different KF architectures in case of faults**

| | EKF | | UKF | |
|---|---|---|---|---|
| Max Position error RMS in case of fault: | Position [m] | Speed [m/s] | Position [m] | Speed [m/s] |
| 1) KF down | 197 | 2.24 | 198 | 8.6 |
| 2) PLL down | 7.35 | 1.72 | 7 | 2.1 |
| 3) random sats loss | 6.98 | 1.56 | 17.63 | 9.12 |

entire list of faults is reported in Table 4. The application of this sequence allows to understand the effects of each kind of fault. Moreover, the overlap between GNSS and AHRS faults makes the approach conservative.

### A. GNSS model

This section mainly focus around simulation of the GNSS receiver. Fig. 7 shows the capability of the model to simulate a realistic satellite constellation. The relative geometry of the satellites in view acts on the DOP as Fig. 8 provides. The increase on the DOP value associated to the reduction of the satellites in view is clearly visible. Based on the relative position of the receiver and the satellites, the tropospheric delay is evaluated for each satellites affecting the final position accuracy. An example can be seen in Fig. 9.

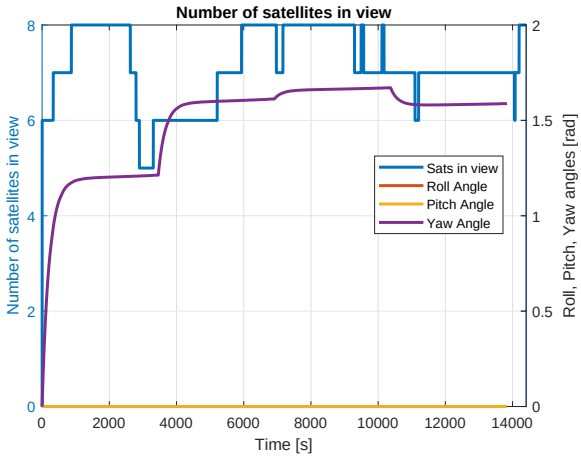


**Fig. 7 Number of satellites in view during a trajectory with no faults occurring.**

The architecture of the output filter on the GNSS receiver affects the accuracy on the final position estimation as shown in Table 5. It must be noticed that those results may vary accordingly to the aircraft motion, type and filter parameters.

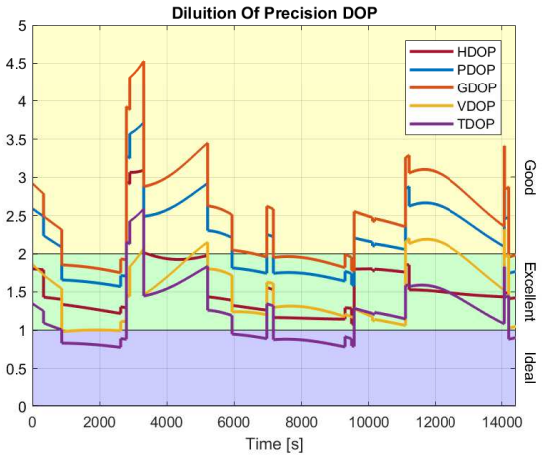


**Fig. 8 DOP trend during the same trajectory as Fig. 7.**

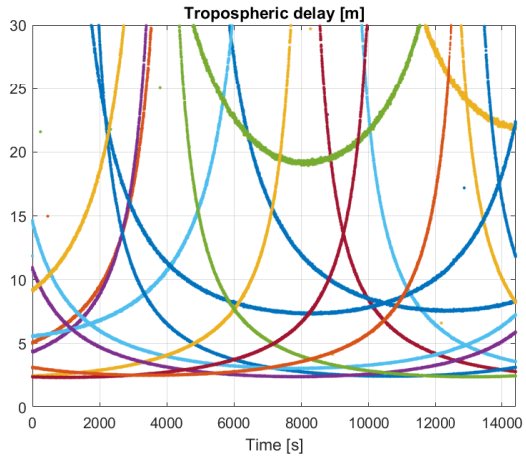


**Fig. 9 Tropospheric delay for each satellite during a trajectory.**

### B. Background sensor noise

This section shows an example of the position error (RMS value) obtained by the GPS/INS integrated architecture in case of background sensor noise and faults. Fig. 10 provides a comparison between the output of the GPS module, both in terms of linear system inversion and KF, and the output of the integrated architecture.

### C. Operative flight noise

Signal noise figure changes among the different flight phase. An example can be seen in Fig. 11, where an harmonic noise with frequency slightly lower than 2 Hz is clearly visible when the aircraft is kept on the ground. In that case, the source may be a structural vibration, excited by the engine or by the propeller. Even variation on electrical grounding system may influence the output of the AHRS, although the power supply is in direct current. However, the AHRS mounted in the test vehicle is an high-quality equipment and those effect should be considered low. Further analysis showed this harmonic disturbance on angular speed and acceleration measurements for both X, Y and Z Body axes. This might be due to cross-correlation of the signals caused by improper orientation of the platform.

For what concern the accelerometers, a white noise component has been found around -20 dB/Hz, lower for Y axis which is around -25 dB/Hz and higher for Z axis exceeding -20 dB/Hz. On the Z axis, this value changes among the flight phases. Flicker noise for accelerometers is showed only during cruise and some kind of harmonic noise around 1 Hz, 2 Hz has been found during taxi. For what concern rate gyros, a white noise has been measured around -65 dB/Hz for Z axis, and between -60 dB/Hz to -50 dB/Hz for X and Y body axes. A source of harmonic noise is clearly visible

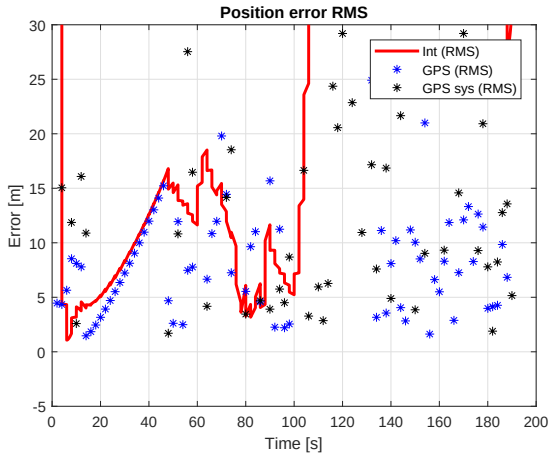


**Fig. 10 Position error RMS with background sensor noise in case of faults.**

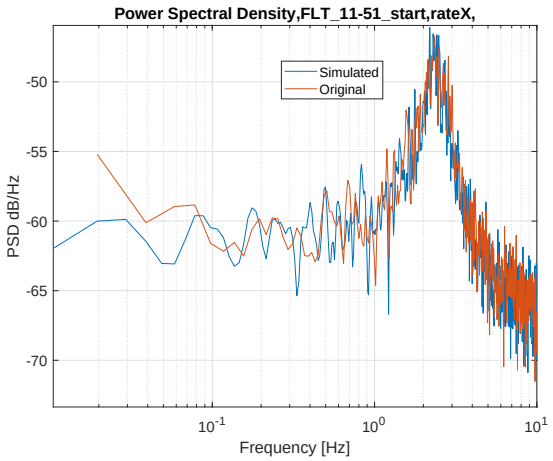


**Fig. 11 PSD for angular rate around X Body**

between 1 Hz and 2 Hz during ground phases with peak around -50 dB/Hz. During cruise and taxi phases, the shape of the PSD changes with a slope greater than 20 dB/decade.

These results could be expected, considering capability of oscillate along Y Body axes respect to X and Z axis of the former where AHRS has been mounted and capability of oscillate around X and Y body axes respect to Z.

It is important to notice a difference of 40 dB/Hz between the white noise power spectrum with only the sensor background noise and the one applying the operative flight noise. A commercial comparison between several sensors showed that the background noise is not one of the feature more correlated with the equipment cost. Hence, background noise itself does not remarkably affect the output of an integrated GPS/INS architecture. At the same time, a good multi-sensor data-fusion technique could make the difference.

In Fig. 12 the output of the integrated architecture and GPS position estimation are compared in case of flight noise and faults.

### D. Smart-ADAHRS response

Previous sections describes the simulator, showing some results to demonstrate its general capability. As previously mentioned, the first aim of the model was to test the Smart-ADAHRS in case of faults and with realistic noise on the input signals. Smart-ADAHRS has been trained and tested in the simulated environment previously depicted. Results showed a good robustness in case of faults and realistic noise on the input signals. Actually, the only fault able to strongly affect the output of the equipment was a null output on the inertial sensors. A temperature ramp applied to the

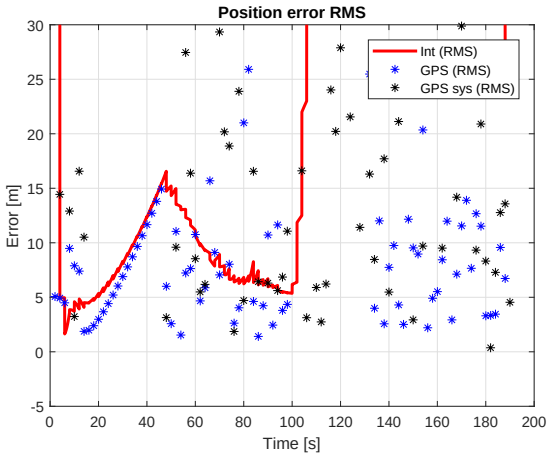


**Fig. 12 Position error RMS with flight noise in case of faults.**

**Table 6 Flight scenario used for training and test sets**

| **Maneuvers** | **Total time** [s] |
|---|---|
| Elevator step | 2200 |
| Elevator step (different trim conditions) | 2200 |
| Ailerons step | 2200 |
| Rudder step | 2200 |
| Mixed elevator and ailerons step | 2200 |
| Sawtooth glides | 1660 |
| Stall | 1630 |
| Trim | 2200 |
| Mixed maneuver | 1070 |

accelerometers can affect the output as well, if the sensor tested has an high temperature sensitivity. However, it should be considered that a properly designed KF could face this kind of failures.

Training and test sets have been built according to the experience gained in this project. Briefly, the training set should cover the maximum portion of the unit hypercube described by the domain of the function to approximate. It is practically impossible to train on an infinite training set so the training set should be representative of the problem. Table 6 shows the flight scenarios simulated.

Moreover, it is very hard to decide the characteristics of the sensors to test. In fact, the complete architecture is made of several parts integrated between each other. This integration tends to affect the signals, to counter noises and faults, and eventually to introduce behavior hard to predict and replicate. It is not practical to test all various configurations, even automatically. Hence, various tests have been conducted together with an analysis of the available commercial sensors, and the configuration reported in Table 7 and Table 8 has been eventually determined, where g stands for g-force, not for grams.

Eventually, 36 simulations have been obtained, 18 with only background noise acting on the sensors, 18 with flight

**Table 7 GNSS sensor configuration tested**

| | |
|---|---|
| Update time interval | 2 s |
| Clock accuracy | 500 ns RMS |
| Frequency accuracy | 0.3 Hz |

**Table 8 Inertial and Air Data sensor configuration tested**

| | Accelerometers | Gyroscopes | Magnetometers | Pressure sensors |
|---|---|---|---|---|
| Bandwidth [Hz] | 40 | 100 | 20 | 10 |
| Non-linearity [%] | 5 | 5 | 5 | 5 |
| Range | ± 2 g | ±125 deg/s | ±180 deg | ±50 hPa |
| Cross-axis sensitivity [%] | 5 | 5 | 5 | - |
| Max scale factor temp. sens. [%/K] | 1 | ± 0.2 | ± 0.5 | ± 0.5 |
| Max bias temp. sens. | ±4 mg/K | ±0.5 deg/s/K | ±0.5 deg/K | ±0.5 Pa/K |
| Max bias | ±300 mg | ±50 deg/s | 0 | 2 hPa |
| Threshold and ADC resolution | 1 mg | 0.001 deg/s | 0.001 deg | 10 Pa |

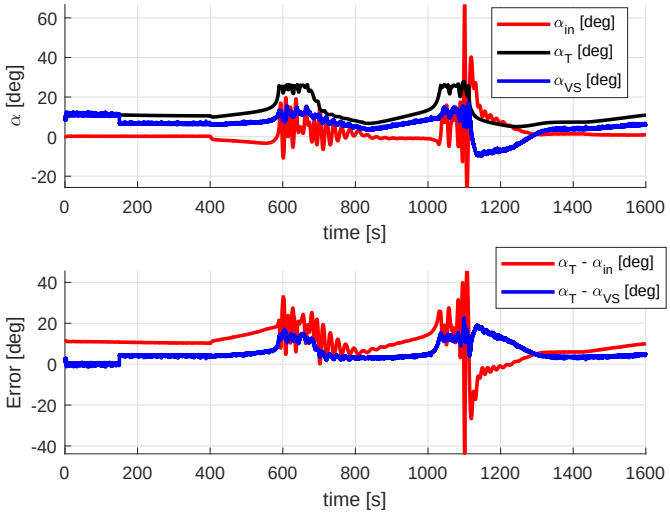


**Fig. 13 Smart-ADAHRS output example in case of flight noise and faults during stall maneuvers (subscripts $VS$, $T$ and $in$ stand respectively for *Virtual Sensor*, *True angle* and *initial estimation*).**

noise. Another simulation lasting only 100 s has been conducted with greater sensibility on temperature faults.

The performance of the algorithm are in accordance with previous findings. The final error distribution has an higher standard deviation than in case of ideal signals. Moreover, in case of flight noise the spread on the error distribution is accentuated. This effect of the noise is in line with initial hypotheses. Actually, the error distribution is close to be normally distributed and this was also encountered in previous studies led on real flight data.

In case of fault injection, as Fig. 13 provides, the only fault that clearly affects the output of the virtual sensor is the null output occurring on the accelerometers. In that case, the value of $\Delta\alpha$ is not correct and the final error reaches 5.4° in case of background noise and 4.5° in case of flight noise. It is interesting to notice that, in case of the stall maneuver, the final error $\alpha_T - \alpha_{VS}$ is still lower than the one obtained by the initial approximation $\alpha_T - \alpha_{in}$. Hence, the NN is still trying to fill the gap, even with two of the input signals ($n_x$ and $n_y$) altered. However, average final error of that extent must be considered unacceptable for this kind of equipment. Fig. 14 shows a detail of the first 180 s, when the faults enlisted in Table 4 are injected. Shaded areas represents the time interval in which the faults are simulated. Except for the first 4 s, the time needed by the GNSS to fix, the virtual sensor does not show any degradation during any GNSS-related faults. Even the temperature slope, injected at 50 s, does not imply any increase on the final error results. In order to show that it is not covered by the flight noise, the same situation is repeated on Fig. 15 in case of background noise. Except for some peaks occurring before the GNSS fix, the error trend is confirmed. To check the effect of a temperature slope on the inertial sensors, a proper simulation has been conducted. A slope of 2 K/s has been applied from 0 s. Flight noise has been applied and to enhance the effect, the temperature sensitivity of the accelerometers was

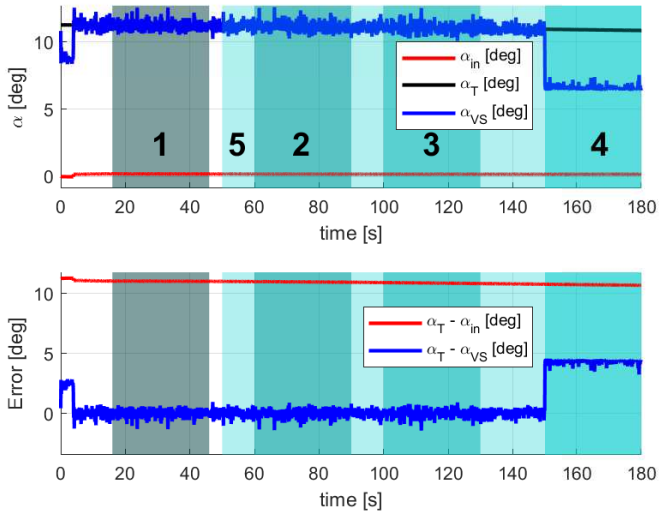


**Fig. 14 Detail of Fig. 13, shaded areas correspond to faults listed in Table 4 (subscripts $VS$, $T$ and $in$ stand respectively for *Virtual Sensor*, *True angle* and *initial estimation*)**

increased of 2 order of magnitude to $0.02\,\mathrm{K}^{-1}$. In this case, the error increases up to 5° in 100 s. However, the value set for the temperature sensitivity must be considered very high.

Some remarks on the integration filters must be considered. During the GNSS faults, the KF propagates the dynamic model equation using the inertial measurements only. This seems to be sufficient for the NN to evaluate the correct $\Delta\alpha$. In fact, a good multi-sensor data fusion technique must be considered the cornerstone of this kind of equipment. Properly designed, a good KF can also avoid temperature issues up to some extent.

## V. Conclusion

A way to estimate the sensitivity analysis for virtual sensors has been shown. The importance of this design phase has been described as a way to help the commercial application of the virtual sensors. This paper shows how to develop a detailed simulated environment, able to replicate typical sensor noises and faults of inertial and air data sensors, together with a detailed GNSS receiver model. Using this kind of analysis, prior information of stability of the algorithm and robustness to fault injection can be determined. Moreover, technical requirements for the preceding sensors can be defined. This analysis, together with the proposed simulator, has been applied to study the virtual sensor for aerodynamic angles called Smart-ADAHRS. Possible limitations of this analysis can be the number of parameters that must be set and the time needed for the simulation. However, the results can still be obtained with a personal laptop. Final results showed which are the most influencing faults that can happen on the preceding sensors. Specifically, a good robustness has been observed on the GNSS faults (unlock of the PLL, partial or total lost of the satellites in view or stop on the updating of the KF) if applied for a limited time. Null output of the inertial sensors prevents the algorithm to work correctly, and temperature related faults can affect the system, if the temperature sensitivity is high (around 2 order of magnitudes higher than COTS sensors). Possible solutions for these faults have also been depicted.

## Acknowledgments

The authors would like to thank Ing. Nando Groppo srl and Politecnico di Milano for their collaboration during the flight test campaign.

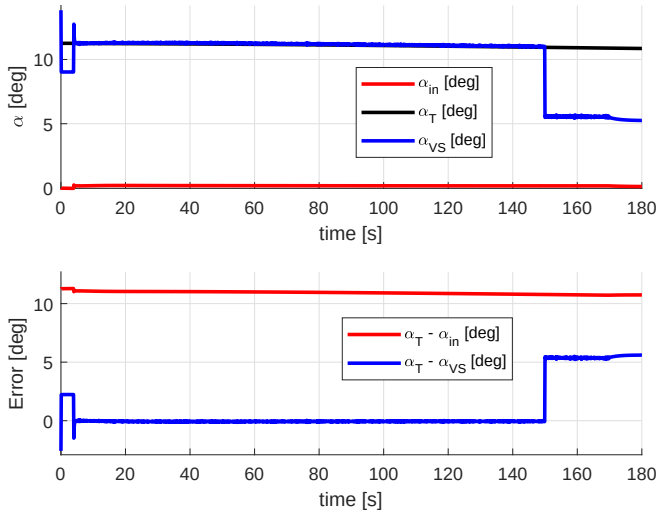


**Fig. 15 Detail of the first $180\,\mathrm{s}$ of a stall maneuver with fault injection (same condition of Fig. 14) with only background noise (subscripts $VS$, $T$ and $in$ stand respectively for *Virtual Sensor*, *True angle* and *initial estimation*)**

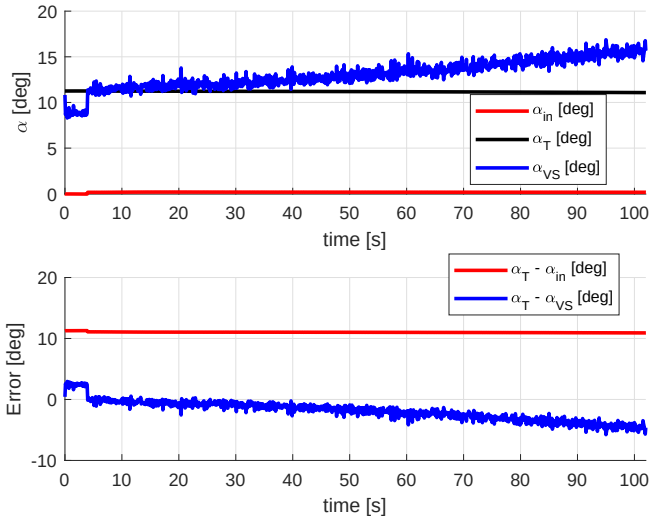


**Fig. 16 Smart-ADAHRS response in case of a temperature increase on the accelerometers of $2\,\mathrm{K/s}$ with an high temperature sensitivity of $0.02\,\mathrm{K}^{-1}$ (subscripts $VS$, $T$ and $in$ stand respectively for *Virtual Sensor*, *True angle* and *initial estimation*)**

# References


[1] Samy, I., and Gu, D.-W., *Lecture Notes in Control and Information Sciences*, Springer-Verlag Berlin Heidelberg, 2011. doi:10.1007/978-3-642-24052-2, URL http://bib.tiera.ru/DVD-030/Francis{_}B.A.{_}A{_}cource{_}in{_}H{_}Control{_}Theory{_}(1987)(en)(156s).pdf.

[2] Palma, G., Scognamiglio, O., and Lavorgna, M., "Low Cost Virtual Pressure Sensor," *SAE Technical Paper*, SAE International, 2004, pp. 1–15. doi:10.4271/2004-01-1367, URL http://dx.doi.org/10.4271/2004-01-1367.

[3] Yu, Y., Woradechjumroen, D., and Yu, D., "Virtual surface temperature sensor for multi-zone commercial buildings," *Energy Procedia*, Vol. 61, 2014, pp. 21–24. doi:10.1016/j.egypro.2014.11.896, URL http://dx.doi.org/10.1016/j.egypro.2014.11.896.

[4] Gertler, J. J., "Survey of model-based failure detection and isolation in complex plants," *IEEE Control Systems Magazine*, Vol. 8, No. 6, 1988, pp. 3–11. doi:10.1109/37.9163.

[5] Isermann, R., "Model-based fault-detection and diagnosis - Status and applications," *Annual Reviews in Control*, Vol. 29, No. 1, 2005, pp. 71–85. doi:10.1016/j.arcontrol.2004.12.002, URL http://www.sciencedirect.com/science/article/pii/S1367578805000052.

[6] Samy, I., Postlethwaite, I., and Gu, D. W., "Survey and application of sensor fault detection and isolation schemes," *Control Engineering Practice*, Vol. 19, No. 7, 2011, pp. 658–674. doi:10.1016/j.conengprac.2011.03.002, URL http://dx.doi.org/10.1016/j.conengprac.2011.03.002.

[7] Isermann, R., and Ballé, P., "Trends in the application of model-based fault detection and diagnosis of technical processes," *Control Engineering Practice*, Vol. 5, No. 5, 1997, pp. 709 – 719. doi:https://doi.org/10.1016/S0967-0661(97)00053-1, URL http://www.sciencedirect.com/science/article/pii/S0967066197000531.

[8] Oliveira, J. C. M., Pontes, K. V., Sartori, I., and Embiruçu, M., "Fault Detection and Diagnosis in dynamic systems using Weightless Neural Networks," *Expert Systems with Applications*, Vol. 84, No. Supplement C, 2017, pp. 200 – 219. doi:https://doi.org/10.1016/j.eswa.2017.05.020, URL http://www.sciencedirect.com/science/article/pii/S0957417417303366.

[9] Gertler, J. J., "Survey of Model-Based Failure Detection and Isolation in Complex Plants," *IEEE Control Systems Magazine*, Vol. 8, No. 6, 1988, pp. 3–11. doi:10.1109/37.9163.

[10] Goupil, P., Dayre, R., and Brot, P., "From theory to flight tests: Airbus Flight Control System TRL5 achievements," *IFAC Proceedings Volumes*, Vol. 47, No. 3, 2014, pp. 10562 – 10567. doi:http://dx.doi.org/10.3182/20140824-6-ZA-1003.02547, URL http://www.sciencedirect.com/science/article/pii/S147466701643291X, 19th IFAC World Congress.

[11] Kooli, M., and Di Natale, G., "A survey on simulation-based fault injection tools for complex systems," *Proceedings - 2014 9th IEEE International Conference on Design and Technology of Integrated Systems in Nanoscale Era, DTIS 2014*, 2014. doi:10.1109/DTIS.2014.6850649.

[12] Kooli, M., and Di Natale, G., "A survey on simulation-based fault injection tools for complex systems," *2014 9th IEEE International Conference on Design Technology of Integrated Systems in Nanoscale Era (DTIS)*, 2014, pp. 1–6. doi:10.1109/DTIS.2014.6850649.

[13] Ziade, H., Ayoubi, R., and Velazco, R., "A Survey on Fault Injection Techniques," *The International Arab Journal of Information Technology*, Vol. 1, No. 2, 2004, pp. 171–186. doi:10.1.1.167.966.

[14] Sabatini, R., Moore, T., and Hill, C., "A New Avionics-Based GNSS Integrity Augmentation System: Part 1 – Fundamentals," *Journal of Navigation*, Vol. 66, No. 3, 2013, p. 363–384. doi:10.1017/S0373463313000027.

[15] Sabatini, R., Moore, T., and Hill, C., "A New Avionics-Based GNSS Integrity Augmentation System: Part 2 – Integrity Flags," *Journal of Navigation*, Vol. 66, No. 4, 2013, p. 501–522. doi:10.1017/S0373463313000143.

[16] Garro, A., Tundis, A., and Chirillo, N., "System reliability analysis: a Model-Based approach and a case study in the avionics industry," *Proceedings of the 3rd Air and Space International Conference (CEAS)*, 2011, pp. 24–28.

[17] Garro, A., and Tundis, A., "A model-based method for system reliability analysis," *Proceedings of the 2012 Symposium on Theory of Modeling and Simulation-DEVS Integrative M&S Symposium*, Society for Computer Simulation International, 2012, p. 2.

[18] Lerro, A., Battipede, M., and Gili, P., "Sistema e procedimento di misura e valutazione di dati aria e inerziali," , 2013. Patent No. TO2013A000601.

[19] Battipede, M., Gili, P., Lerro, A., Caselle, S., and Gianardi, P., "Development of Neural Networks for Air Data Estimation: Training of Neural Network Using Noise-Corrupted Data," *3rd CEAS Air & Space Conference, 21st AIDAA Congress*, 2011, pp. 1–10.

[20] Battipede, M., Cassaro, M., Gili, P., and Lerro, A., *Novel Neural Architecture for Air Data Angle Estimation*, Springer Berlin Heidelberg, Berlin, Heidelberg, 2013, pp. 313–322. doi:10.1007/978-3-642-41013-0_32, URL http://dx.doi.org/10.1007/978-3-642-41013-0_32.

[21] Battipede, M., Gili, P., and Lerro, A., *Neural Networks for Air Data Estimation: Test of Neural Network Simulating Real Flight Instruments*, Springer Berlin Heidelberg, Berlin, Heidelberg, 2012, pp. 282–294. doi:10.1007/978-3-642-32909-8_29, URL http://dx.doi.org/10.1007/978-3-642-32909-8_29.

[22] Lerro, A., Battipede, M., Gili, P., and Brandl, A., "Survey on a Neural Network for Non Linear Estimation of Aerodynamic Angles," *Proceedings of the 2017 Intelligent Systems conference (IntelliSys)*, Vol. Unico, IEEE, 2017, pp. 929–935.

[23] Lerro, A., Battipede, M., Gili, P., and Brandl, A., "Advantages of Neural Network Based Air Data Estimation for Unmanned Aerial Vehicles," *International Journal of Mechanical, Aerospace, Industrial, Mechatronic and Manufacturing Engineering*, Vol. 11, No. 5, 2017, pp. 1016 – 1025. URL http://waset.org/Publications?p=125.

[24] Lerro, A., Battipede, M., Gili, P., and Brandl, A., "Comparison Between Numerical Results and Operative Environment Data on Neural Network for Air Data Estimation," *PROCEEDINGS of the 6th CEAS Air and Space Conference Aerospace Europe 2017*, Vol. Unico, George Bogdan GHERMAN, 2017, pp. 1–20.

[25] Lerro, A., Battipede, M., Brandl, A., Gili, P., Rolando, A. L. M., and Trainelli, L., "Test in Operative Environment of an Artificial Neural Network for Aerodynamic Angles Estimation," *Proceedings of the 28th Society of Flight Test Engineers (SFTE) European Chapter Symposium*, Vol. Unico, 2017, pp. 1–12.

[26] Grewal, M. S., Weill, L. R., and Andrews, A. P., *Global Positioning Systems, Inertial Navigation, and Integration*, Wiley-Interscience, 2001.

[27] Schmidt, G. T., and Phillips, R. E., "INS/GPS Integration Architectures," Tech. rep., Massachussetts Institute of Technology, 2010.

[28] De Vivo, F., Battipede, M., Gili, P., and Brandl, A., "Ill-conditioned problems improvement adapting Joseph covariance formula to non-linear Bayesian filters," *WSEAS Transactions on Electronics*, Vol. 7, edited by W. Press, 2016, p. 18–25. doi:10.13140/RG.2.1.3027.0960.

[29] De Vivo, F., Brandl, A., Battipede, M., and Gili, P., "Joseph covariance formula adaptation to Square-Root Sigma-Point Kalman filters," *Nonlinear Dynamics*, Vol. 88, No. 3, 2017, pp. 1969–1986. doi:10.1007/s11071-017-3356-x, URL https://doi.org/10.1007/s11071-017-3356-x.

[30] Noori, H. R., *Preisach Models*, Springer Berlin Heidelberg, Berlin, Heidelberg, 2014, pp. 21–32. doi:10.1007/978-3-642-38218-5_3, URL https://doi.org/10.1007/978-3-642-38218-5_3.

[31] Mayergoyz, I. D., and Friedman, G., "Generalized Preisach model of hysteresis," *IEEE Transactions on Magnetics*, Vol. 24, No. 1, 1988, pp. 212–217. doi:10.1109/20.43892.

[32] Ikhouane, F., and Rodellar, J., "On the hysteretic Bouc-Wen model," *The name of the journal*, 2005.

[33] Wang, L. X., and Willatzen, M., "Nonlinear Dynamical Model for Hysteresis Based on Nonconvex Potential Energy," *Journal of Engineering Mechanics*, Vol. 133, 2007. doi:https://doi.org/10.1061/(ASCE)0733-9399(2007)133:5(506).

[34] *IEEE Standard Specification Format Guide and Test Procedure for Single-Axis Interferometric Fiber Optic Gyros*, 2008.

[35] El-Sheimy, N., Hou, H., and Niu, X., "Analysis and Modeling of Inertial Sensors Using Allan Variance," *IEEE Transactions of Instrumentation and Measurement*, Vol. 57, No. 1, 2008, pp. 140–149. doi:10.1109/TIM.2007.908635.

[36] Sullivan, D. B., Allan, D. W., Howe, D. A., and Walls, F. L., "Characterization of Clocks And Oscillators," Tech. rep., National Institute of Standards and Technology, 1974.

[37] Ta-Kang, Y., Cheinway, H., Guochang, X., Chuan-Sheng, W., and Chien-Chih, L., "Determination of global positioning system (GPS) receiver clock errors: impact on positioning accuracy," *Measurement Science and Technology*, Vol. 20, No. 7, 2009, pp. 1–7. doi:10.1088/0957-0233/20/7/075105, URL http://stacks.iop.org/0957-0233/20/i=7/a=075105.

[38] Weinbach, U., and Schon, S., "GNSS receiver clock modeling when using high-precision oscillators and its impact on PPP," *Advances In Space Research*, Vol. 47, 2011, pp. 229–238. doi:10.1016/j.asr.2010.06.031, URL http://linkinghub.elsevier.com/retrieve/pii/S0273117710004497.

[39] Cybenko, G., "Approximation by superpositions of a sigmoidal function," *Mathematics of Control, Signals and Systems*, Vol. 2, No. 4, 1989, pp. 303–314. doi:10.1007/BF02551274, URL https://doi.org/10.1007/BF02551274.

[40] Hornik, K., "Approximation capabilities of multilayer feedforward networks," *Neural Networks*, Vol. 4, No. 2, 1991, pp. 251 – 257. doi:https://doi.org/10.1016/0893-6080(91)90009-T, URL http://www.sciencedirect.com/science/article/pii/089360809190009T.

[41] Bishop, C. M., *Neural Networks for Pattern Recognition*, Clarendon Press Oxford, 1995.

[42] Bishop, C. M., *Pattern Recognition and Machine Learning*, Springer-Verlag New York, 2006.

[43] Park, M., "Error Analysis and Stochastic Modeling of MEMS based Inertial Sensors for Land Vehicle Navigation Applications," Master's thesis, University Of Calgary, 2004.

[44] Kay, S. M., *Modern spectral estimation : theory and application*, Englewood Cliffs, N.J. : Prentice Hall, 1988.

[45] Niell, A. E., "Global mapping functions for the atmosphere delay at radio wavelengths," *Journal of Geophysical Research: Solid Earth*, Vol. 101, No. B2, 1996, pp. 3227–3246. doi:10.1029/95JB03048, URL http://dx.doi.org/10.1029/95JB03048.